



## **In situ observation of a strong diurnal warming event in the Labrador sea undetected by satellites**

Title	In situ observation of a strong diurnal warming event in the Labrador sea undetected by satellites
Author(s)	Hauser, Simon F.;ten Doeschat, Anneke;Ward, Brian;Esters, Leonie
Publication Date	2026-01-10
Publisher	American Geophysical Union;Wiley
Repository DOI	<a href="https://doi.org/10.1029/2025JC022918">https://doi.org/10.1029/2025JC022918</a>

# In Situ Observation of a Strong Diurnal Warming Event in the Labrador Sea Undetected by Satellites



### Key Points:

- A diurnal warming event of 1.5°C in the top 2 m of the ocean was detected in the Labrador Sea with the ASIP microstructure instrument
- Coincident data from nine different satellites, the most prevalent detection method, showed no evidence of the event due to cloud cover
- Diurnal warming has the potential to occur more frequently than satellites observe based on heuristic criteria from this in situ data set

### Supporting Information:

Supporting Information may be found in the online version of this article.

### Correspondence to:

L. Esters and B. Ward,  
lesters@uni-bonn.de;  
bward@universityofgalway.ie

### Citation:

Hauser, S. F., ten Doeschate, A., Ward, B., & Esters, L. (2026). In situ observation of a strong diurnal warming event in the Labrador Sea undetected by satellites. *Journal of Geophysical Research: Oceans*, 131, e2025JC022918. <https://doi.org/10.1029/2025JC022918>

Received 23 MAY 2025

Accepted 20 DEC 2025

### Author Contributions:

**Conceptualization:** Brian Ward, Leonie Esters

**Data curation:** Brian Ward

**Formal analysis:** Simon F. Hauser, Anneke ten Doeschate

**Funding acquisition:** Brian Ward

**Investigation:** Anneke ten Doeschate

**Methodology:** Simon F. Hauser, Brian Ward

**Project administration:** Brian Ward

**Resources:** Brian Ward, Leonie Esters



**Software:** Simon F. Hauser, Brian Ward, Leonie Esters

**Supervision:** Brian Ward, Leonie Esters

**Visualization:** Simon F. Hauser, Leonie Esters

© 2026. The Author(s).

This is an open access article under the terms of the [Creative Commons Attribution License](https://creativecommons.org/licenses/by/4.0/), which permits use, distribution and reproduction in any medium, provided the original work is properly cited.

Simon F. Hauser<sup>1</sup>, Anneke ten Doeschate<sup>2</sup>, Brian Ward<sup>3</sup> , and Leonie Esters<sup>1</sup> 

<sup>1</sup>Institute of Geosciences, Meteorology Section, University of Bonn, Bonn, Germany, <sup>2</sup>Rockland Scientific International Inc., Victoria, BC, Canada, <sup>3</sup>AirSea Laboratory and Ryan Institute, School of Natural Sciences, University of Galway, Galway, Ireland

**Abstract** Diurnal warming (DW) at the ocean surface occurs when there is a combination of solar heating in the absence of vertical mixing typically derived from wind stress. DW has been well described, mostly from satellite data, but also with some in situ observations. Evidence of DW has mostly been restricted to the subtropics, and there are very few reports of DW at northerly latitudes. We present here observations of a DW event of 1.5°C confined to the upper 2 m in the Labrador Sea at >55°N. These measurements were conducted with the Air-Sea Interaction Profiler (ASIP), an upwardly rising, ocean microstructure instrument. Cloud cover obscured the ocean surface to passive remote-sensing instruments and as a result no evidence of this particular DW event was available from the nine independent satellite products that were analyzed. Therefore, the event would have gone undetected without the deployment of ASIP at precisely this time and location. The ASIP observations were used to derive a heuristic set of criteria for potential occurrences of DW in the Labrador Sea region: (a) shortwave radiation above 600 W m<sup>-2</sup> and (b) 10-m wind speed below 4 m s<sup>-1</sup>. These criteria were subsequently applied to ~40 years of the ERA5 reanalysis product indicating that DW events in the Labrador Sea have the potential to occur more frequently than satellites observe. Attaching microstructure temperature sensors on Argo floats would provide a more accurate assessment of the occurrence of DW events globally as well as their effect on surface mixing rates.

**Plain Language Summary** This study presents observations of a strong increase in the temperature of the upper 2 m of the ocean in the Labrador Sea. This is known as diurnal warming, as it occurs during the day when adequate solar heating is available. Diurnal warming also requires sufficiently low wind speeds to prevent mixing of the deeper colder waters, which eradicates the temperature gradients observed here. Diurnal warming can be important for the exchange of heat and carbon between the ocean and the atmosphere, which is a major contributor to climate regulation. At lower latitudes, diurnal warming has been observed extensively mostly from satellite observations, but there are very few reports closer to the Arctic. Because the measurement region was largely obscured by clouds, satellites were unable to detect the diurnal warming event observed here, which was performed with an autonomous ascending profiler. Combining these observations with a climatological reanalysis data set, we derived conditions for the potential for diurnal warming to occur and conclude that diurnal warming could occur more frequently than satellites can observe in the Labrador Sea region. We also suggest that microstructure temperature sensors be attached to Argo floats, so that these diurnal warming events can be more readily detected.

## 1. Introduction

Shortwave radiation (SWR) influences the ocean's energy budget and is therefore a major determinant of the Earth's climate. Under conditions of high SWR combined with low wind speed, several reports have shown a significant increase in the sea surface temperature (SST). This upper ocean thermal stratification is known as diurnal warming (DW), and the corresponding depth over which the DW penetrates is the diurnal warm layer (DWL).

The amount of SWR reaching the ocean surface is influenced by cloud cover (Webster et al., 1996). Clouds affect the surface energy budget through their interactions with long- and shortwave radiation, which have competing effects on the sea surface temperature (SST). On the one hand, clouds re-emit longwave radiation from the Earth causing a warming of the sea surface. On the other hand, clouds absorb and scatter shortwave radiation, thereby preventing surface warming (Wielicki et al., 1995). On a global scale, the cooling effect from scattering the

**Writing – original draft:** Simon F. Hauser, Leonie Esters  
**Writing – review & editing:** Anneke ten Doeschate, Brian Ward, Leonie Esters

shortwave radiation exceeds the warming effect from re-emitting the longwave radiation with the result that clouds have a net cooling effect (Loeb et al., 2009). Ward (2006) showed that the appearance of clouds can cause an immediate cooling of the ocean surface under very low winds.

The temperature difference  $\Delta T$  across the DWL is defined as  $\Delta T = T_{SST} - T_{FND}$  where  $T_{SST}$  is the sea surface temperature and  $T_{FND}$  is the foundation temperature, defined as the minimum SST during a 24 hr period, which typically occurs just before local sunrise (Donlon et al., 2002). Values of  $\Delta T$  range from  $O(0.1^\circ\text{C})$  (Kawai & Wada, 2007; Kennedy et al., 2007; Merchant et al., 2008; Stuart-Menteth et al., 2003) to several degrees celsius (Eastwood et al., 2011; Fairall et al., 1996; Merchant et al., 2008; Soloviev & Lukas, 1997; Ward, 2006; Wick & Castro, 2020) with extreme values reaching  $>6^\circ\text{C}$  (Gentemann et al., 2008; Jia et al., 2023). The depth of the DWL has been observed to reach several meters (Fairall et al., 1996; Soloviev & Lukas, 1997) and a shallower DWL results in a larger  $\Delta T$ . As the depth of the DWL depends on the level of turbulent mixing, increased turbulence can erode the well-stratified DWL and cause it to deepen (Gentemann et al., 2003; Jia et al., 2023). Turbulence can be increased by wind stress and ocean surface waves particularly through wave breaking (Belcher et al., 2012; Hogan et al., 2025).

DW has been shown to affect air-sea heat fluxes, causing potential biases in their determination of up to  $60\text{ W m}^{-2}$  (Fairall et al., 1996; Ward, 2006). DW modifies the concentration of aqueous  $\text{CO}_2$  through the solubility of the gas in seawater, and knowledge of the diurnal variability of SST is essential for correct estimates of air-sea gas exchange (Bellenger & Duvel, 2009; Kettle et al., 2009; McNeil & Merlivat, 1996; Ward et al., 2004; Woolf et al., 2016). DW also drives the air-sea buoyancy flux, which is an important factor for turbulence in the ocean surface boundary layer (Belcher et al., 2012; Esters et al., 2018; Lombardo & Gregg, 1989). The stabilizing buoyancy flux due to near-surface stratification arising from DW suppresses mixing within the ocean mixed layer (Brainerd & Gregg, 1993; Flament et al., 1994; Kukulka et al., 2013; Merchant et al., 2008; Noh et al., 2009; Price et al., 1986; Sutherland et al., 2016; Sverdrup et al., 1942). Large-eddy simulations have shown that Langmuir circulation is weakened under surface warming conditions and can fully break down in cases of sufficiently strong DW (Min & Noh, 2004). DW also inhibits near-surface turbulence, which is the principal process for controlling air-sea exchange of heat and carbon (Asher & Pankow, 1986; Esters et al., 2017; Lamont & Scott, 1970; Tokoro et al., 2008; Zappa et al., 2007). DW is therefore an important process for upper ocean dynamics and air-sea exchange.

The largest differences in diurnal temperature are found in the western Pacific warm pool (Soloviev & Lukas, 1997) and the Indian Ocean (Kennedy et al., 2007). Further areas of DW interest are the marginal seas around Japan where large diurnal SST variations have been observed (Kawai & Kawamura, 2000, 2002), the South China Sea (Hsu et al., 2024), or the midlatitudes such as the North Sea (Gentemann et al., 2008; Merchant et al., 2008). There have also been studies, albeit fewer that have focused on higher latitudes. Through a combination of different satellite products, Eastwood et al. (2011) observed DW cycles, which reached SST amplitudes of several degrees  $^\circ\text{C}$  at latitudes up to  $80^\circ\text{N}$ . Jia et al. (2023) used saildrones to study DW in the Bering and Chukchi Seas and observed several large DW events with amplitudes of up to  $5^\circ\text{C}$ . They also reported two DW events where the DWL persisted throughout the night in conditions of low wind, midnight sun, and warm air at the surface, which suppressed heat loss (Jia et al., 2023).

Although there are several reports of in situ DW observations (e.g., Anderson & Riser, 2014; Castro et al., 2014; Kawai et al., 2006; Soloviev & Lukas, 1997; Webster et al., 1996; Zeiden et al., 2024), many studies utilize satellite data (Castro et al., 2014; Clayson & Weitlich, 2005, 2007; Kawai et al., 2006; Stuart-Menteth et al., 2003; Wick & Castro, 2020). Satellite observations retrieve SST through radiometer instruments that measure either in the microwave or infrared wavelengths (Gentemann et al., 2008; Stuart-Menteth et al., 2003). Polar orbiting satellites provide a day- and nighttime observation, which allows for estimates of the global distribution of DW (Kawai & Wada, 2007; Kennedy et al., 2007; Stuart-Menteth et al., 2003). However, estimates of DW based on satellites equipped with infrared sensors are unavailable in regions that are obscured by clouds, which is a major limitation in ascertaining the frequency of occurrence of DW events globally.

Higher latitudes are prominent for cloud formation and the Arctic is covered by clouds for 80% of the year (Beesley & Moritz, 1999). The Labrador Sea is a region that has significant cloud cover (Warren et al., 1988), and there have been no reports of DW events here. In order to look for evidence of DW, we deployed the autonomous upwardly rising Air-Sea Interaction Profiler (ASIP) during the AR7W repeat line cruise on the Canadian Coast Guard Ship (CCGS) Hudson in May 2010 (Wain et al., 2015). We discovered a highly localized yet significant

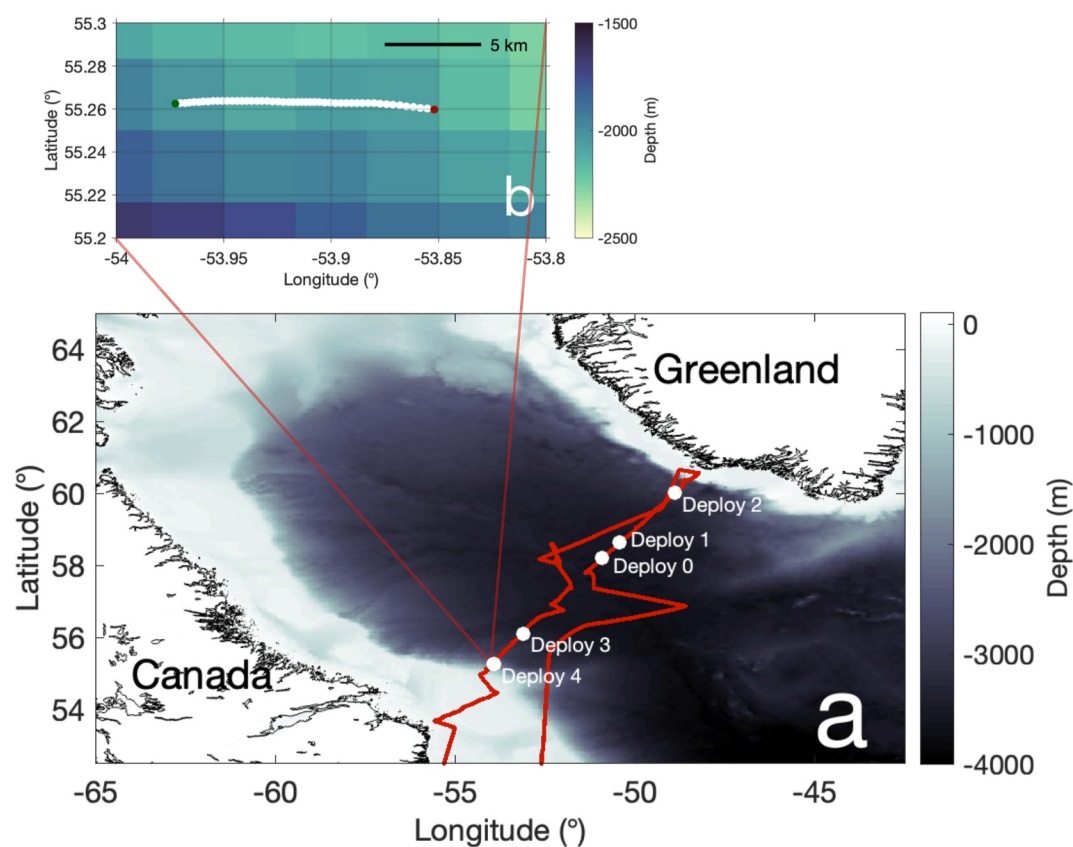


**Figure 1.** (a) Cruise track of the CCGS Hudson (red) from the departure port of St. John's, returning to Halifax via the Strait of Belle Isle. The ASIP deployments in the open ocean across the Labrador Sea are shown in white. Deployment 4 is used for this paper. None of the other ASIP deployments showed any evidence of DW. (b) The ASIP track (white) for deployment 4 showing the start (green) and end (red) positions. ASIP moved due east and was in ocean depths  $>2000$  m throughout the deployment.

DW event with a  $\Delta T$  of  $>1^\circ\text{C}$  at a latitude of  $55^\circ\text{N}$ , which was not detected by any of the satellites dedicated to monitoring SST. Here, Section 2 details the observations and data that we utilize. Section 3 presents the results and discussion with our conclusions in Section 4.

## 2. Observations

### 2.1. In Situ

The AR7W cruise is a repeat line conducted annually by the Bedford Institute of Oceanography across the Labrador Sea of the (Wain et al., 2015; Yashayaev & Loder, 2016). In May 2010, the AR7W cruise was carried out on the CCGS Hudson, which departed the port of St. John's on May 12 and returned to Halifax on May 30 (Figure 1).

One of the motivations for the AR7W cruise was to investigate the existence of DW in the Labrador Sea, and the ASIP was deployed for this purpose. ASIP provides microstructure measurements of the upper 100 m of the ocean; it is an autonomous upwardly rising profiler designed to investigate small-scale ocean surface boundary layer processes (for further details see Ward et al., 2014). The profiler is equipped with a set of sensors including microstructure temperature, conductivity, shear, and photosynthetically active radiation (PAR). The dissipation rate of turbulent kinetic energy  $\epsilon$  can be estimated from the microstructure shear measurements. One of the main advantages of using ASIP for this DW study is that it can resolve the small scale temperature to the depth of the sub-skin ( $T_{\text{subskin}}$ ), which is coincident of the base of the molecular boundary layer (Donlon et al., 2002; Ward & Donelan, 2006).

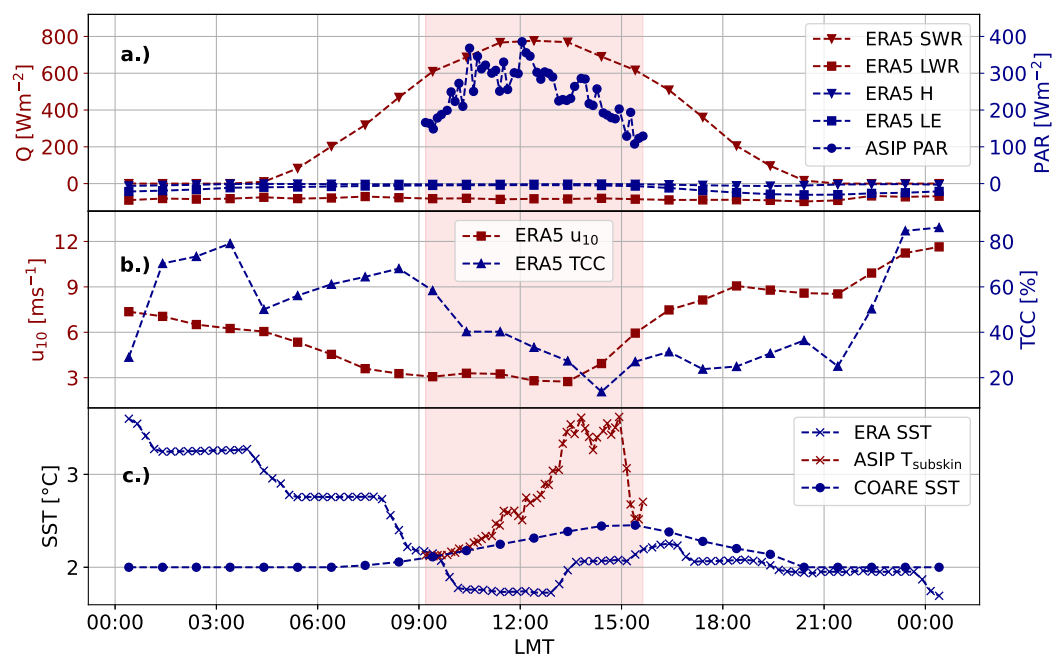


**Figure 2.** Time series of the meteorological conditions during the ASIP deployment on 23 May 2010 (indicated by the shaded red area): (a) ERA5 shortwave radiation (SWR), longwave radiation (LWR), sensible heat flux (H), latent heat flux (LE), and ASIP photosynthetically active radiation (PAR) at the ocean surface. (b) ERA5 wind speed ( $u_{10}$ ) and total cloud coverage (TCC). (c) ERA SST, ASIP subskin temperature ( $T_{\text{subskin}}$ ), and SST derived from COARE 3.6 using a 5 m baseline temperature of  $2^{\circ}\text{C}$  and ERA5 forcing parameters. Local mean time (LMT) is such that local noon is when the sun is at its highest point.

ASIP was deployed six times (Figure 1a) during the AR7W cruise (Figure 1a does not show one of the deployments, which was located south of Newfoundland), but only a single deployment showed evidence of DW albeit a significant event. Wain et al. (2015) presented data from the third deployment (Figure 1) of an internal breaking wave detected with the ASIP shear probes, which drove the turbulence levels 2–3 orders of magnitude above the background. Deployment 4 (Figure 1b) occurred on 23 May 2010 at  $55.26^{\circ}\text{N}$ ,  $53.9^{\circ}\text{W}$ .

ERA5 reanalysis data (Hersbach et al., 2023) provided by the European Center for Medium-Range Weather Forecasts (ECMWF) was used to achieve a record of the relevant atmospheric forcing parameters. Shortwave radiation (SWR), longwave radiation (LWR), sensible heat flux (H), latent heat flux (LE), total cloud cover (TCC), and 10-m wind speed ( $u_{10}$ ) were extracted to match the position of the ship (Figure 2). As ERA5 only has daily SST values publicly available, which are interpolated to each hour of the day, a tailored data set for the AR7W cruise track provided by the ECMWF was used.

The ASIP data set consists of 50 profiles sampled every 7 min with a pause of 10–15 min after every fifth profile to conduct an iridium message transfer to relay the position of the instrument with some basic instrument diagnostic data (for further details see Ward et al., 2014). Although these profiles reached a maximum depth of 100 m, in this DW study, we limit the focus to the upper 5 m for the temperature measurements, as the DW event affected the temperature distribution in the upper 5 m (Figures 3a and 3b). For the dissipation rate, only the upper 14 m are shown based on the maximum estimated mixed layer depth (Figure 3c).

## 2.2. Satellite

To compare the in situ measurements of SST with satellite data, SST products from polar orbiting and geostationary satellites were used. In May 2010, fourteen polar-orbiting satellite instruments were operational and provided data to derive SST, eight of which had high-quality SST products available for the Labrador Sea. There was also one geostationary satellite (GOES-13) whose data were utilized here.

All satellite instruments operated in the infrared range except for the Advanced Microwave Scanning Radiometer for Earth Observing System (AMSR-E) aboard NASA's Aqua satellite. An estimate of the amplitude of DW

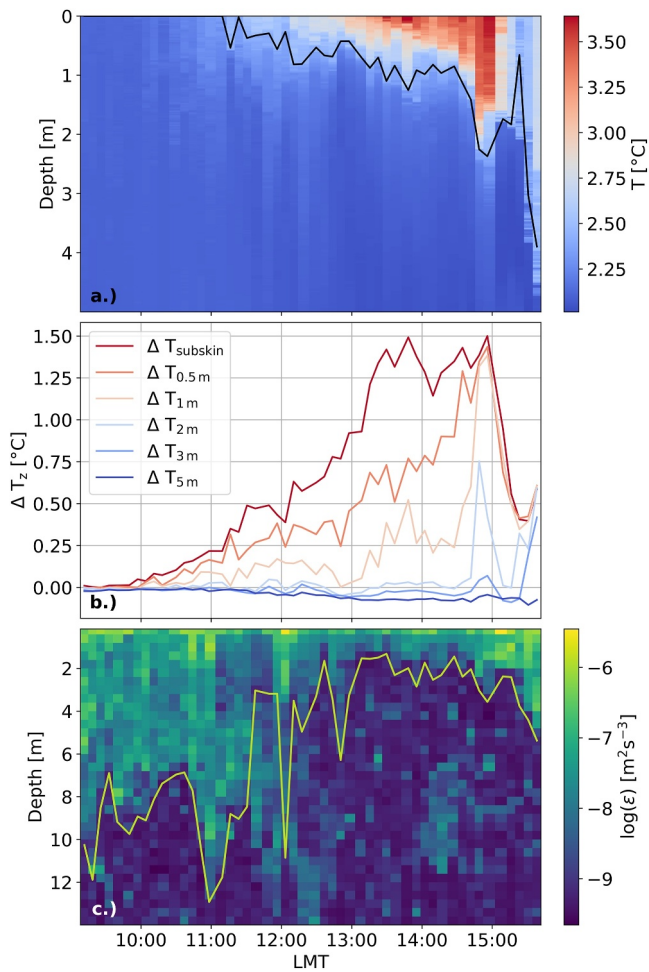


**Figure 3.** (a) Temporal distribution of temperature over the upper 5 m showing the depth of the DWL ( $z_{DWL}$ ; black). (b) Temperature amplitudes  $\Delta T_z$  at increasing depth levels with respect to  $T_{FND}$ . (c) Temporal evolution of the dissipation rate of turbulent kinetic energy ( $\epsilon$ ) over the upper 14 m of the ocean. Also shown is an estimate of the mixed layer depth based on the dissipation profile (MLD; green).

events can be obtained from the data of polar orbiting satellites by comparing the SSTs of two consecutive overpasses: one at nighttime conditions and one at daytime conditions. Geostationary satellites can provide hourly estimates of SST and therefore capture DW events. Table 1 provides an overview of SST data available for 22–24 May 2010 in the Labrador Sea taken as the bounding box with lower-left and upper-right coordinates as  $[65^\circ\text{W}, 52.5^\circ\text{N}]$  and  $[42.5^\circ\text{W}, 65^\circ\text{N}]$ , respectively (the same bounding box as in Figure 1a).

All SST data are Level-3 Collated (L3C) products with the exception of AMSR-E where Level-3 Uncollated (L3U) data were used. L3 data are gridded data sets based on a single overpass (L3U) or created by combining multiple overpasses in space and time (L3C). For NASA's Aqua satellite, AMSR-E data (Remote Sensing Systems, 2014), AIRS data (AIRS project, 2019), and data from the Moderate-resolution Imaging Spectroradiometer (MODIS) was used (NOAA CoastWatch, 2024). For the Terra satellite, only MODIS data were utilized (NOAA CoastWatch, 2024). For the satellites instrumented with AVHRR/3, data from NOAA-18, NOAA-19, and MetOp-A were considered (Embury, 2024). Furthermore, AATSR data from ENVISAT are included in Table 1 (Embury et al., 2019). See Table A1 in the appendix for definitions of all abbreviations used.

Data from the NOAA-15, NOAA-16 and NOAA-17 satellites and the European Remote Sensing Satellite 2 (ERS-2) are excluded from Table 1, as technical problems occurred before May 2010 influencing the quality of SST products (Embury et al., 2024; Merchant et al., 2019). Data provided by the Advanced Spaceborne Thermal Emission and Reflection Radiometer (ASTER) onboard NASA's Terra satellite were used to derive SST products (Chen et al., 2013), but there was no SST product available for the Labrador Sea based on ASTER data only. SST was also derived based on Chinese Ocean Color and Temperature Scanner (COCTS) data from the Hai Yang 1B (HY-1B) satellite, but there was no data available for the Labrador Sea in 2010 (Liu et al., 2022). Therefore, the ASTER and COCTS data were not included in Table 1.

The large difference between AIRS SST and AMSR-E SST close to the ASIP location can be explained by the different bin centers ( $55.375^\circ\text{N}, 53.875^\circ\text{W}$  for AMSR-E and  $55^\circ\text{N}, 54^\circ\text{W}$  for AIRS) and the different grid sizes of the products in combination with the high spatial SST gradient observed (see Figure 4). For example,  $\text{SST} = 0.90^\circ\text{C}$  was derived for daytime conditions on 23 May at  $54.875^\circ\text{N}, 53.875^\circ\text{W}$  based on AMSR-E data, which are close to

$\text{SST} = 1.10^\circ\text{C}$  obtained for daytime conditions on 23 May at  $55^\circ\text{N}, 54^\circ\text{W}$  based on AIRS data. The observed lateral SST gradients could in principle also be observed as a change in background water temperature with ASIP, as the instrument could drift into water masses with different characteristics during the measurement period. But this is not the case, as the observed background water temperature at up to 5 m depth is uniformly distributed (Figure 3a).

Of the geostationary satellites, seven were initially considered, five of which were part of the Geostationary Operational Environmental Satellite (GOES) program. Of these, only GOES-13 was fully operational and covered the Labrador Sea at a zenith angle smaller than  $75^\circ$  in May 2010 (Ocean and Sea Ice Satellite Application Facility (OSI SAF), 2015). GOES-13 is therefore included in Table 1. For the remaining two, Meteosat-9 (Longitude  $3.5^\circ\text{E}$ ) and Himawari-7 (Longitude  $145^\circ\text{E}$ ), the Labrador Sea was not in the field of view (Maturi et al., 2008).

### 3. Results and Discussion

#### 3.1. ASIP Observations of Diurnal Warming Event

The motivational data set for this study was acquired with the ASIP autonomous profiling instrument (see Section 2) over a period of about 6.5 hr on 23 May 2010 in the Labrador Sea. Figure 2 presents the atmospheric

**Table 1**  
*Overview of Satellite-Based SST Data Available for 22–24 May 2010 in the Labrador Sea (65°W, 52.5°N, 42.5°W, 65°N)*

Satellite	Instrument	Grid size	Coverage on 23 May [%]	SST at ASIP location	Local time of equator crossing
Aqua	MODIS	0.02°	28.26	22.05. 3.90° Night 23.05. No Data 24.05. 4.17°C Day	13:30
Terra	MODIS	0.02°	28.54	22.05. No Data 23.05. 3.24°C Night 24.05. No Data	10:30
Aqua	AIRS	1°	79.82	22.05. 0.73°C asc 0.16°C dsc 23.05. 1.10°C asc 24.05. No Data	13:30
Aqua	AMSR-E	0.25°	60.22	22.05. No Data 23.05. 4.35°C 24.05. 3.45°C	13:30
NOAA-18	AVHRR/3	0.05°	16.86	22.05. 3.60°C Night 23.05. No Data 24.05. 3.70°C Day	14:00
NOAA-19	AVHRR/3	0.05°	17.50	22.05. 2.75°C Day 3.52°C Night 23.05. No Data 24.05. No Data	13:30
ENVISAT	AATSR	0.05°	5.31	22.05. No Data 23.05. No Data 24.05. No Data	10:00
MetOp-A	AVHRR/3	0.05°	51.55	22.05. 2.12°C Day 23.05. 2.14°C Night 24.05. No Data	09:30
GOES-13	IMAGER	0.05°	3.62	22.05. 3.19°C 05:00 3.43°C 06:00 23.05. No Data 24.05. No Data	Geostationary

*Note.* The coverage is determined as the number of available data pixels divided by the total number of nonland pixels in the observation region. For the Moderate-resolution Imaging Spectroradiometer (MODIS) instruments, the coverage was calculated based on Level-2 Pre-processed (L2P) flags, with sea ice considered as land pixels. For GOES-13, the coverage is given as the average coverage of all hours on 23 May 2010. The differences in coverage and SST data points are caused by differences between the grid sizes, instruments, and local times of overpasses. All abbreviations are defined in the appendix in Table A1.

forcing parameters: shortwave radiation (SWR), longwave radiation (LWR), sensible heat flux (H), latent heat flux (LE), total cloud cover (TCC), and 10-m wind speed ( $u_{10}$ ). All ERA5 data are shown for the full 24-hr period of the day of deployment. Figure 2 also shows a time series of surface PAR as an in situ measure of the availability of light at the surface and SST ( $T_{\text{subskin}}$ ) from ASIP, which is taken as the ASIP temperature closest to the surface (Ward, 2006).

The net heat flux was primarily driven by SWR with only minor contributions from outgoing LWR and latent and sensible heat fluxes. The surface SWR reached a maximum of  $777 \text{ W m}^{-2}$ , which occurred midway during the ASIP deployment. The PAR surface data from ASIP and the SWR data indicate that the measurement period from 09:12 to 15:38 local mean time (LMT) is almost symmetrical around local noon. The PAR is lower than the SWR because the wavelength range considered is smaller. The ERA5 wind speed was initially up to  $7 \text{ m s}^{-1}$  but

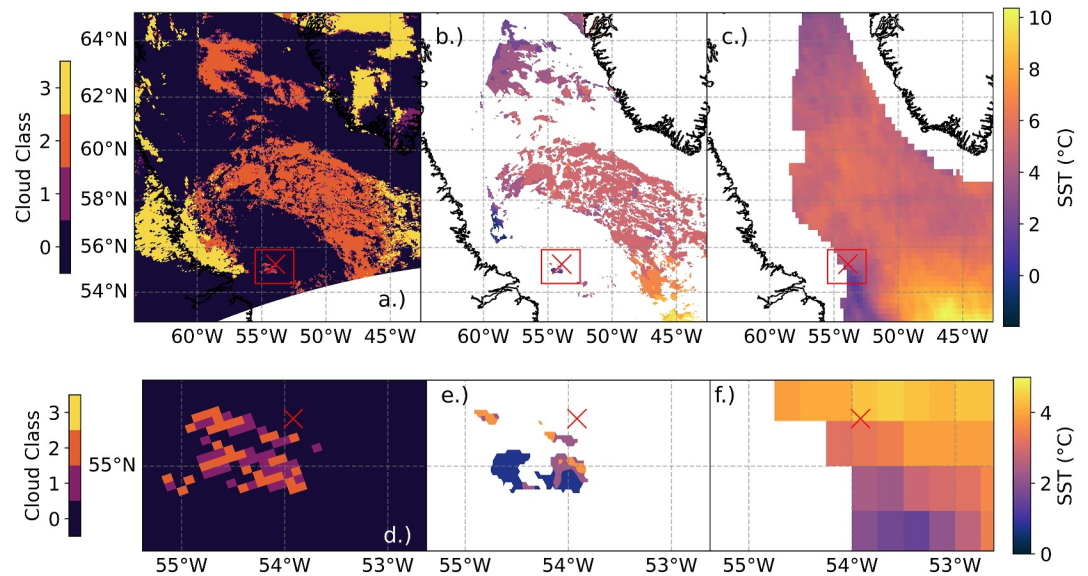


**Figure 4.** (a) Aqua MODIS Level-2 (L2) cloud mask, (b) Aqua MODIS Level-3 (L3) SST data, and (c) AMSR-E (L3) SST data for 23 May 2010 in the Labrador Sea (Ackerman, 2017; NOAA CoastWatch, 2024; Remote Sensing Systems, 2017). The red cross indicates the ASIP position at (55.26°N, 53.9°W) where SST = 4.35°C was measured by AMSR-E at around 12:30 p.m. local time during the ASIP deployment. The cloud classification assigns the following categories: 0—Cloudy, 1—Uncertain, 2—Probably Clear, and 3—Confident Clear.

decreased to  $<3 \text{ m s}^{-1}$  toward the end of the ASIP measurement period. TCC was 40 % or less during the period of interest.

At the beginning of the ASIP measurement period (09:12 LMT), there is a well-mixed isothermal layer reflecting pre-warming conditions (Figure 3a), and the ASIP  $T_{\text{subskin}}$  differs from the ERA5 SST by less than  $0.1^\circ\text{C}$  (Figure 2c). However, after the SWR reaches  $600 \text{ W m}^{-2}$  at around 09:30 LMT (Figure 2a),  $\Delta T_{\text{subskin}}$  quickly begins to increase and is already significantly larger than the temperature in 1 m depth after an hour.  $\Delta T_{\text{subskin}}$  then increases further steadily until it reaches a maximum value of  $1.5^\circ\text{C}$  at around 13:50 LMT (Figure 3b). The  $\Delta T_{\text{subskin}}$  varies between 1.2 and  $1.5^\circ\text{C}$  until 14:55, whereupon a mixing event erodes the stratification and removes the temperature gradients in the upper 3 m. The depth of the DWL ( $z_{\text{WL}}$ ) shown in Figure 3a is determined with a threshold temperature and follows a fixed isotherm, that is, based on  $T_{\text{FND}}$  (A. J. Matthews et al., 2014).  $T_{\text{FND}}$  is the well-mixed SST before the onset of warming. Here,  $T_{\text{FND}} = 2.1^\circ\text{C}$  was used, which corresponds to the minimum  $T_{\text{subskin}}$  measured with ASIP. For this study,  $z_{\text{WL}}$  was estimated from the isotherm  $T = T_{\text{FND}} + 0.2(T_{\text{max}} - T_{\text{FND}}) = 2.42^\circ\text{C}$  (A. J. Matthews et al., 2014) where  $T_{\text{max}}$  denotes the maximum  $T_{\text{subskin}}$  measured with ASIP.

Thermal stratification of the surface waters commences very soon after the deployment. Here, the subskin temperature heats up faster than the temperatures at depths below (Figure 3b). Up to the time at which  $T_{\text{subskin}}$  reaches a maximum value, the temperature at 1 m depth ( $T_{1\text{m}}$ ) increases gradually in accordance with the increase of  $T_{\text{subskin}}$ . However,  $T_{1\text{m}}$  remains  $0.3\text{--}1.1^\circ\text{C}$  cooler than  $T_{\text{subskin}}$  highlighting the prevailing stratification. At 14:30, the temperature at 1 m and below increases with a steep gradient indicating that warm surface waters were mixed downward. The temperature gradients disappear quickly, showing that this mixing event resulted in the sudden removal of stratification. The timescale of this mixing makes it plausible that it was caused by a wind gust that led to the collapse of the well-stratified warm layer at the end of the ASIP time series. DWLs are highly sensitive to wind fluctuations. Depending on the degree of stratification, an increase in  $u_{10}$  of only  $1 \text{ m s}^{-1}$  is sufficient to erode the DWL (Jia et al., 2023; Stuart-Menteth et al., 2005). Sudden wind bursts at the time of maximal diurnal SST can mix the water within the top meter deeper into the ocean. This mixing causes a reduction in temperature close to the surface, but an increase in temperature in deeper layers, as observed here with ASIP (Figure 3b). Wind gusts also determine the timescales on which surface water is mixed to greater depths (Giglio et al., 2017).

The dissipation rate of turbulent kinetic energy ( $\epsilon$ ; Figure 3c) indicates the availability of mixing, which is relatively low due to the diminished wind speeds. The mixed layer depth (MLD), defined as the depth of active turbulent mixing, is determined using a threshold of  $10^{-9} \text{ m}^2 \text{ s}^{-3}$  (Giunta & Ward, 2022; Sutherland et al., 2014). The dissipation data reflect wind and buoyancy-driven mixing into the upper ocean. The MLD starts out at about 10 m indicating a remnant of nighttime convection. After 11:00 LMT, it decreases rapidly to about 3 m when the solar insolation overcomes heat loss at the surface. A similar daily cycle of turbulence was observed in the subtropics with a day-night cycle of re-stratification and convection (Sutherland et al., 2016). At 12:00, there is a short increase in turbulence and the MLD deepens for less than 20 min, which could be caused by a local increase in wind speed that is not reflected in the ERA5 data (Figure 2).

Subsequently, the MLD shoals to about 1.5–3 m and the DW event continues to develop. The MLD remains at this depth until about 15:15, when a sudden increase in turbulence erodes the stratification until the end of available data. This indicates that the wind suddenly increased, thereby eroding the DWL, given that wind is the main source of turbulence into the upper ocean. The significant height of combined wind and swell waves from ERA5 (see Figure S4 in Supporting Information S1) indicates wave heights lower than 2 m for the whole measurement period, further evidence for wind as the main driver of turbulence. Toward the end of the measurement period (15:38 LMT), an increase in wind speed from about 3 to 6  $\text{m s}^{-1}$  can also be seen in the ERA5 data (Figure 2). The steady decrease in PAR toward the end of the measurement period did not cause the observed increase in turbulence, as it occurs sharply (Figure 3c) and PAR is only slightly lower than at the beginning of the observation period where the DW event starts to develop. Around 21:00, after the end of the ASIP measurement, the wind speed increases further to 11.5  $\text{m s}^{-1}$  and the cloud cover also abruptly increases from 25 to about 85 %.

The strength of this DW event can be explained by the combination of weak winds and large SWR leading to a shallow MLD. In general, about half of the solar irradiance is absorbed in the uppermost 1 m of the ocean (Kara et al., 2005). Although the ERA5 SST and the ASIP  $T_{\text{subskin}}$  agree at the beginning of the ASIP measurement period, the development of this DW event is not captured by ERA5 SST data (Figure 2). The COARE 3.6 estimation of the DW amplitude (Figure 2c) was derived using a 5 m baseline temperature of 2°C and ERA5 forcing parameters, excluding the skin effect (Fairall et al., 2003). Although COARE reproduces the development of a DW event, the maximum amplitude of 0.45°C is about a degree less than observed and is reached 1.5 hr later. These differences could be due to the ERA5 input being provided at an hourly resolution only or the ERA5 forcing parameters not accurately reflecting all conditions at the measurement site.

### 3.2. Coincident Satellite Observations

The satellite observations had only partial availability of SST data due to cloud cover. This is not atypical, as the average TCC in the Labrador Sea in May is around 80% (Warren et al., 1988). Among the data from infrared radiometers, SST for 23 May for daytime conditions at the ASIP position is only available from the AIRS, SST = 1.10°C (see Table 1). However, there is no AIRS data available for nighttime conditions (neither on 23 May nor on 24 May) so the DW amplitude cannot be estimated from AIRS data. The grid size for this data is  $1^\circ \times 1^\circ$  (111 km  $\times$  64 km at 55°N), which is the largest in Table 1. For the other SST products with a smaller grid size (0.02°–0.05°) based on infrared measurements, there is no data available for daytime conditions on 23 May at the ASIP position due to cloud cover. However, there is AMSR-E data available at a grid size of 0.25° as the instrument operates in the microwave range and can measure SST in cloudy conditions when there is no precipitation (Gentemann, 2014). But the AMSR-E SST product is only available in daily resolution; therefore, no DW amplitude could be derived. In conclusion, it is not possible to estimate the DW amplitude at the ASIP position on 23 May 2010 based on SST products provided by polar orbiting satellites.

Geostationary satellites could in principle provide hourly SST data at the ASIP position. For the IMAGER instrument on board of GOES-13, which was the only platform covering the Labrador Sea on 23 May 2010, no data is available at the ASIP position due to cloud cover (see Table 1). Therefore, SST from geostationary satellites could not be utilized to estimate the DW amplitude.

The SST coverage of AMSR-E and the MODIS on board of the Aqua satellite as well as the MODIS cloud mask are shown in Figure 4. AMSR-E is chosen out of the instruments in Table 1, as it is the only one with SST available for daytime conditions at the ASIP position with a grid size  $<1^\circ$  and has a relatively high spatial coverage, although SST is not available near the coast (Gentemann, 2014). The Aqua MODIS data were selected because it provides the highest spatial resolution available and is directly comparable to the AMSR-E data, as both

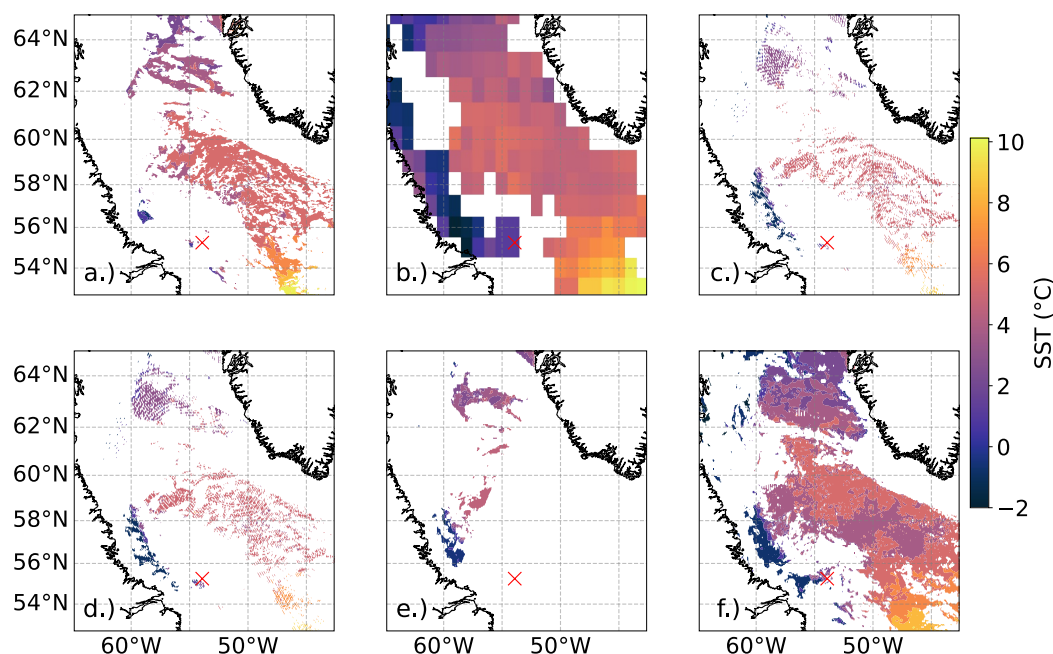


**Figure 5.** Level-3 (L3) SST data products for 23 May 2010 in the Labrador Sea: (a) Terra MODIS, (b) Aqua AIRS, (c) NOAA-18 AVHRR/3, (d) NOAA-19 AVHRR/3, (e) ENVISAT AATSR, and (f) MetOp-A AVHRR/3. The red cross indicates the ASIP position at (55.26°N, 53.9°W). Note the different local times of equator crossings and spatial resolutions for the various instruments (see Table 1). SST based on data from the AVHRR/3 instrument on MetOp-A has a high spatial coverage, but the local time of equator crossing is at 09:30; therefore, the data do not reflect the conditions during the observed DW event.

instruments were operating on NASA's Aqua satellite (see Figure 5 for the SST coverage of other instruments considered in Table 1). As can be seen from the MODIS cloud mask data (Figure 4a), the Southern Labrador Sea was largely obscured by clouds on 23 May 2010, but there was a gap in the cloud cover south-west of the ASIP position. In a total area of about 2,500 km<sup>2</sup>, 30 pixels (5 km × 5 km per pixel) were marked as probably clear and 31 were marked as uncertain. In May, the solar elevation at local noon in the Labrador Sea (e.g., 55°N) is only about 55–56°; therefore, it appears that the SWR reached the measurement location through this highly localized pinhole gap in the cloud cover, which enabled the formation of the observed DW event.

### 3.3. Potential for Diurnal Warming Occurrences

The satellite and in situ observations show that DW events with a considerable amplitude of  $\Delta T = 1.5^\circ\text{C}$  can form in regions with localized gaps in the cloud cover in the Labrador Sea. Therefore, it follows that there is a higher potential for DW events to form at the ocean surface than detected by satellite products. We define this diurnal warming potential (DWP) as the percentage of days in a month at which a certain requirement to the meteorological conditions is fulfilled in an angular bin ( $0.25^\circ \times 0.25^\circ$ ) in the Labrador Sea.

Based on the ERA5 reanalysis data (see Figure 2), we suggest that the interplay of the following conditions enabled the development of the observed DW event: (a) shortwave radiation higher than  $600 \text{ W m}^{-2}$  and (b) 10-m wind speed lower than  $4 \text{ m s}^{-1}$ . These conditions should not be interpreted as necessary or sufficient for the occurrence of DW in the Labrador Sea in general but can be considered as a rule of thumb. A threshold for  $u_{10}$  of  $<6 \text{ m s}^{-1}$  was applied in the production of several daily blended L4 SST analyzes to exclude DW observations (Wick et al., 2024).

We also considered TCC as a criterion for DWP. The MODIS cloud mask data (see Figure 4a) suggest a higher TCC than the ERA5 reanalysis data. Assuming the percentage of cloudy pixels in a radius of 50 km around the ASIP position is approximated as TCC, the value at 12:30 local time is 83 %, whereas the ERA5 TCC has a value of approximately 20 % (see Figure 2). Because of this discrepancy, no TCC threshold for the formation of the observed DW event based on ERA5 data is used.

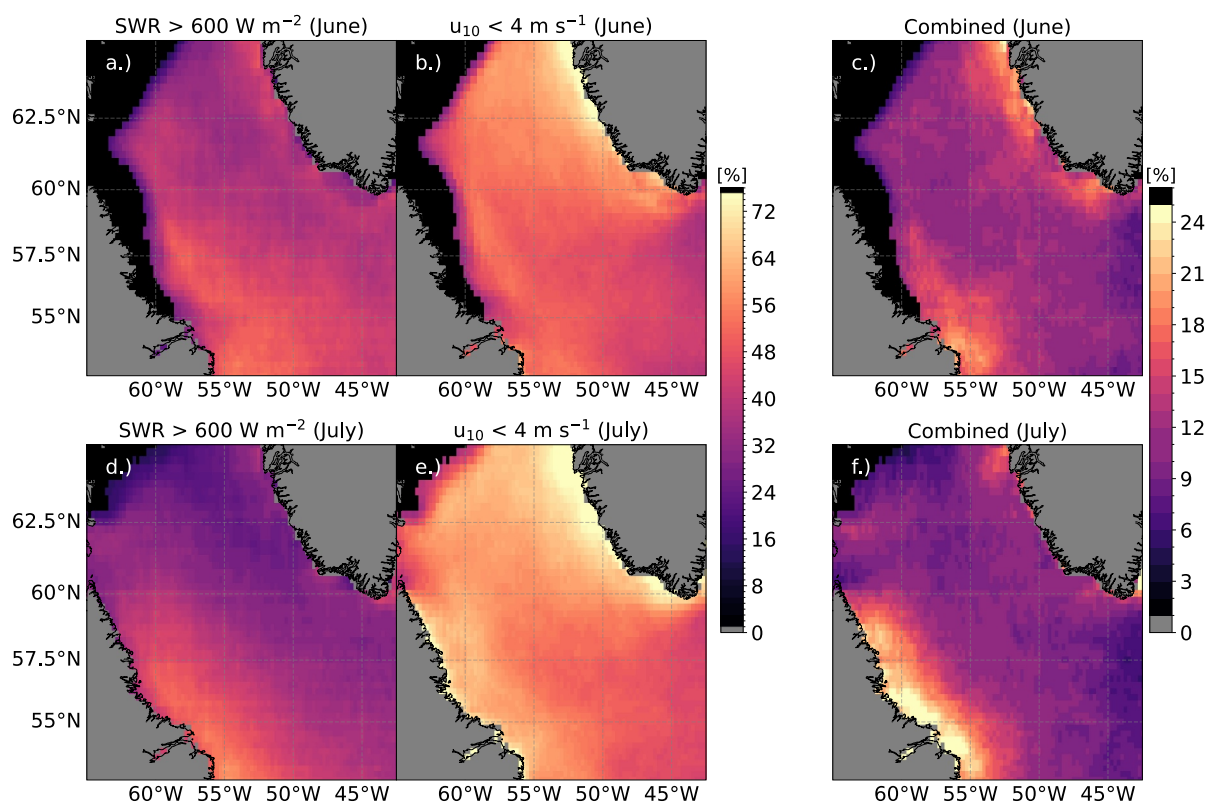


**Figure 6.** Maps showing 40 years (1979–2019) of ERA5 reanalysis data for June in panels (a–c) and July in panels (d–f). Percentage of days when (a) the shortwave radiation (SWR) was higher than  $600 \text{ W m}^{-2}$ , (b) the 10-m wind speed was lower than  $4 \text{ m s}^{-1}$ , and (c) both conditions were fulfilled for at least 1 hr. Panels (d–f) show the same but for July. Land is shown in gray, and areas that are covered with ice more than half of the time are shown in black. Note that panels (a, b, d, e) use different colorbar scales than panels (b, f).

Criteria (i) and (ii) were applied to 40 years (January 1979 to November 2019) of hourly ERA5 reanalysis data (Hersbach et al., 2023) or a total of 14,943 days. As the highest DWP occurs in June and July, we focus on the spatial characteristics of DWP during these months (Figure 6). For a discussion of DWP during the other months, see the supporting information (Figures S1–S3 in Supporting Information S1). Areas that were covered with ice for more than 50 % of the time are omitted (indicated by regions in black in Figure 6). If these two criteria were achieved for at least 1 hr in a day for a given location, then a  $\text{DWP} = 1$  was returned, otherwise the DWP would be zero. A value of 1 hr was chosen because our in situ observations have shown that DW events can evolve significantly within 1 hr in the Labrador Sea (see Figure 3b and the discussion in Section 3.1). This is consistent with the typical timescale for stratification to form due to solar insolation at low to moderate winds in tropical oceans being 1–2 hr (Moulin et al., 2018). A given day at each location is only considered for DWP, if the sea ice coverage is less than 15% for all hours (J. L. Matthews et al., 2020).

Another criterion that could be considered for the DWP is wave height represented by the ERA5 variable describing the significant height of combined wind waves and swell (SWH). Breaking surface waves can induce upper ocean turbulence (Belcher et al., 2012; Hogan et al., 2025), which could erode an existing DWL or inhibit the formation of a DWL. Based on the ERA5 SWH during the ASIP measurement period (see Figure S4 in Supporting Information S1), we applied a criterion of SWH lower than 2 m to 40 years of ERA5 data additionally to criteria (i) and (ii). Averaging over all angular bins, the DWP including the SHW criterion is 92% of the DWP excluding the SWH criterion in June and 96% in July (see Figures S5 and S6 in Supporting Information S1 for details). Therefore, the SWH does not significantly influence the DWP and is not introduced as a third criterion. Provided there is no substantial swell, the influence of the SWH on the DWP is expected to be minor, since  $u_{10}$  and wind wave height are closely coupled.

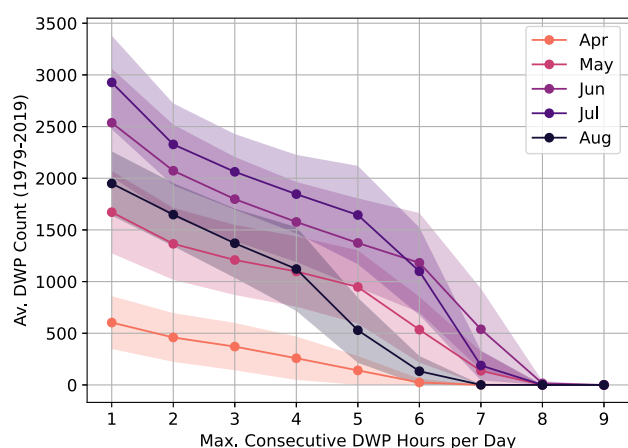


**Figure 7.** Time statistics of DWP: Average DWP count per year for the years 1979–2019 separately for the months April–August and summed up across all angular bins. The DWP count is presented as a function of the maximum number of consecutive hours on the respective day during which the conditions for DWP were met; the shading represents the  $1\sigma$  range of the 40-year average.

For the derivation of the DWP, we assumed that the MLD is typically deeper than the depth of the DWL in the Labrador Sea, such that the effect of initial ocean stratification on the development of DW events can be neglected. Initial ocean stratification could be caused by freshwater input by precipitation or melting sea ice or upwelling and downwelling, for example. The DWL depth is up to a few meters in general, whereas the MLD in the Labrador Sea ranges between 10 and 50 m in summer (Naustvoll et al., 2020) and more than 1 km in winter (Yashayaev & Loder, 2017; Yashayaev et al., 2003). For our observations, Figure 3c shows that the MLD was about 10 m before the onset of warming for the DW event.

SWR at the ocean surface surpasses the threshold of  $600 \text{ W m}^{-2}$  for about 35–50 % of the days in June for most of the Labrador Sea with larger values in the south (Figure 6a). The wind speed fulfills the condition for about 50 % of the days in the central Labrador Sea, 35–50 % in the southeastern Labrador Sea, and more than 75 % close to the coast of Greenland (Figure 6b). In a narrow band along the coast, barrier winds lead to frequent low wind periods (Gorter et al., 2014). The combined conditions are met for around 20 % of the days near the coasts and for about 10 % in the central Labrador Sea (Figure 6c). In the proximity of regions where sea ice is present more than half of the time (black area in Figure 6), the DWP is lower because the corresponding locations are also covered with sea ice for some days in June.

For July, the SWR criterion is fulfilled for fewer days in the northern Labrador Sea compared to June, and the availability of SWR is also lower in the central and southeastern Labrador Sea (Figure 6d). The condition on wind speed is fulfilled for more than 75 % of the days close to the coast of Greenland, for a larger area than in June, and for 65 % to more than 75 % along the coast of Labrador, which is sea-ice free in July (Figure 6e). The combined conditions are met for more than 25 % of the days near the coast of Labrador, for about 10 % in the central Labrador Sea, and for 15–25 % in some areas along the coast near Greenland (Figure 6f). DWP is therefore primarily constrained by the SWR criterion in July.

The DWP derivation counts a day as having a DWP in an angular bin, if the conditions are met for at least 1 hr on that day. But the development of the DW event, particularly the DW amplitude, depends on the maximum number of consecutive hours during which the conditions were met. Figure 7 shows the total DWP count across all angular bins per year, averaged over 40 years, as a function of the maximum consecutive hours of fulfilled conditions on the respective day. Although the DWP counts are highest in June and July, there is also a significant amount of potential DW events in April, May, and August (Figure 7). DW events can potentially occur in March and September but only rarely and only in the southern Labrador Sea (not shown here). Due to a lack of available SWR, there is no DWP from October to February. The number of days on which the conditions are fulfilled for at least four consecutive hours is significant compared to the total average DWP count particularly in May, June, and July (Figure 7), such that DW events with similar magnitudes to the observed event could develop. DW events can be erased quickly by wind fluctuations (Jia et al., 2023; Stuart-Menteth et al., 2005), but they can also be slowly dissolved by surface cooling or freshwater effects. In this case, the characteristic timescale of the process is a few hours (Shcherbina et al., 2019). Therefore, the hourly DWP analysis potentially underestimates the duration of DW events in the case of continuously low winds and a decreasing SWR in the evening.

#### 4. Conclusions

A strong DW event was observed in the Labrador Sea at  $>55^\circ\text{N}$ . Under stable wind conditions, the surface ocean heated by up to  $1.5^\circ\text{C}$  and a well-defined DWL evolved in the uppermost meters of the ocean. This DW event resulted from a combination of a shallow MLD due to low-wind conditions and strong heat flux into the ocean from substantial solar radiation at the specific location of the deployment. As a result, this warm layer restricted mixing in the ocean surface boundary layer.

Based on our observations in combination with the ERA5 reanalysis data, we suggest that the following conditions enabled the development of the DW event: (a) shortwave radiation higher than  $600 \text{ W m}^{-2}$  and (b) 10-m wind speed lower than  $4 \text{ m s}^{-1}$ . According to these conditions and based on ERA5 reanalysis data from 1979 to

2019, localized DW events may have occurred in the Labrador Sea during the local summer due to the highest SWR especially in June and July. Specifically, most parts of the Labrador Sea reached the SWR and  $u_{10}$  critical values for 35 % (30 %) and 45 % (50 %) of the days in June (July), respectively, indicating that the SWR was a higher limiting factor than wind for DWP.

Although there has been little evidence of DW in the Arctic region, Jia et al. (2023) observed 16 significant DW events with amplitudes higher than 2°C using a saildrone in the Bering Sea and Chukchi Sea between 15th of May and 11th of October 2023. The coincident solar radiation did not exceed our defined threshold of 600 W m<sup>-2</sup> for most of these days, which suggests that the threshold might be lower for the Labrador Sea leading to a higher DWP.

The results of this study form an additional argument for the wider application of microstructure sensors in the ocean. Advances in low power electronics and the onboard processing capability of data logging systems make a discussion of adding microstructure sensors to profiling floats used in the Argo program increasingly relevant (Le Boyer et al., 2023; Thierry et al., 2025). Global deployment of microstructure floats can serve the dual purpose of capturing DW events as well as their effect on surface mixing rates.

To explore the extent of DWP further, a comprehensive study is needed that combines satellite and in situ data from various locations. In the Labrador Sea, DWP will likely increase with declining sea ice coverage due to more open water being available especially in coastal regions in April, May, and June.

## Appendix A: Abbreviations

**Table A1**  
*List of Abbreviations*

List of abbreviations	
AATSR	Advanced Along-Track Scanning Radiometer
AIRS	Atmospheric Infrared Sounder
AMSR-E	Advanced Microwave Scanning Radiometer for EOS
ASTER	Advanced Spaceborne Thermal Emission and Reflection Radiometer
AVHRR	Advanced Very High Resolution Radiometer
CCGS	Canadian Coast Guard Ship
COCTS	China Ocean Color and Temperature Scanner
DW	Diurnal Warming
GOES	Geostationary Operational Environmental Satellite
ENVISAT	Environmental Satellite
EOS	Earth Observing System
HY-1B	Hai Yang 1B
L2P	Level-2 Preprocessed
MetOp-A	Meteorological Operational Weather Satellite A
MODIS	Moderate-resolution Imaging Spectroradiometer
MTSAT-2	Japanese Multifunction Transport Satellite—2
NOAA	National Oceanic and Atmospheric Administration
SWH	Significant Height of Combined Wind Waves and Swell
SST	Sea Surface Temperature
SWR	Shortwave Radiation
TCC	Total Cloud Cover

### Conflict of Interest

The authors declare no conflicts of interest relevant to this study.

### Data Availability Statement

This study used ERA5 reanalysis data (Hersbach et al., 2023) downloaded from <https://doi.org/10.24381/cds.adbb2d47>. Furthermore, several different satellite SST products were used (NOAA CoastWatch, 2024; AIRS project, 2019; Remote Sensing Systems, 2014; Embury, 2024; Embury et al., 2019; Ocean and Sea Ice Satellite Application Facility (OSI SAF), 2015). The data used in the study are available at <https://doi.org/10.5281/zenodo.17580777> (Ward & Hauser, 2025) under Creative Commons Attribution 4.0 International License.

### Acknowledgments

SFH thanks the University of Bonn for the internal funding for his PhD position. LE acknowledges support from Formas, the Swedish Research Council for Sustainable Development (2020-02305\_3), and the Bonn Global Collaboration Fund of the University of Bonn, which allowed SFH to visit the AirSea Lab in Galway. BW acknowledges support from Research Ireland under Grant 20/EPSC/3673 with additional funding provided from the European Union's Horizon 2020 Research and Innovation Programme under Grant agreement 821001. We thank P.J. Minnett for providing valuable feedback. We extend our thanks to the Bedford Institute of Oceanography and the captain and crew of the CCGS Hudson for making this study possible. Any requests concerning the data in this paper should be directed to the corresponding author.

### References

- Ackerman, S. (2017). MODIS Atmosphere L2 Cloud Mask Product. NASA MODIS Adaptive Processing System, Goddard Space Flight Center, USA [Dataset]. [https://doi.org/10.5067/MODIS/MYD35\\_L2.061](https://doi.org/10.5067/MODIS/MYD35_L2.061)
- AIRS project. (2019). Aqua/AIRS L3 Daily Standard Physical Retrieval (AIRS-only) 1 degree x 1 degree V7.0, Greenbelt, MD, USA, Goddard Earth Sciences Data and Information Services Center (GES DISC) [Dataset]. <https://doi.org/10.5067/UO3Q64CTTS1U>
- Anderson, J. E., & Riser, S. C. (2014). Near-surface variability of temperature and salinity in the near-tropical ocean: Observations from profiling floats. *Journal of Geophysical Research: Oceans*, 119(11), 7433–7448. <https://doi.org/10.1002/2014JC010112>
- Asher, W., & Pankow, J. F. (1986). The interaction of mechanically generated turbulence and interfacial films with a liquid phase controlled gas/liquid transport process. *Tellus B: Chemical and Physical Meteorology*, 38(5), 305–318. <https://doi.org/10.1111/j.1600-0889.1986.tb00256.x>
- Beesley, J. A., & Moritz, R. E. (1999). Toward an explanation of the annual cycle of cloudiness over the Arctic Ocean. *Journal of Climate*, 12, 395–415. [https://doi.org/10.1175/1520-0442\(1999\)012<textless3C0395:TAEOTA/textgreater3E2.0.CO;2](https://doi.org/10.1175/1520-0442(1999)012<textless3C0395:TAEOTA/textgreater3E2.0.CO;2)
- Belcher, S. E., Grant, A. L. M., Hanley, K. E., Fox-Kemper, B., Van Roekel, L., Sullivan, P. P., et al. (2012). A global perspective on Langmuir turbulence in the ocean surface boundary layer. *Geophysical Research Letters*, 39(18), L18605. <https://doi.org/10.1029/2012GL052932>
- Bellenger, H., & Duvel, J.-P. (2009). An analysis of tropical ocean diurnal warm layers. *Journal of Climate*, 22(13), 3629–3646. <https://doi.org/10.1175/2008JCLI2598.1>
- Brainerd, K. E., & Gregg, M. C. (1993). Diurnal stratification and turbulence in the oceanic surface mixed layer – 1. Observations. *Journal of Geophysical Research*, 98(C12), 22645–22656. <https://doi.org/10.1029/93jc02297>
- Castro, S. L., Wick, G. A., & Buck, J. J. H. (2014). Comparison of diurnal warming estimates from unpumped Argo data and SEVIRI satellite observations. *Remote Sensing of Environment*, 140, 789–799. <https://doi.org/10.1016/j.rse.2013.08.042>
- Chen, C.-Q., Zheng, S.-S., & Tang, S. (2013). A new method for retrieval of SST from ASTER image. In *34th Asian Conference on Remote Sensing 2013, ACRS 2013* (Vol. 2, pp. 1516–1522).
- Clayton, C. A., & Weitlich, D. (2005). Diurnal warming in the tropical Pacific and its interannual variability. *Geophysical Research Letters*, 32(21), L21604. <https://doi.org/10.1029/2005GL023786>
- Clayton, C. A., & Weitlich, D. (2007). Variability of tropical diurnal sea surface temperature. *Journal of Climate*, 20(2), 334–352. <https://doi.org/10.1175/jcli3999.1>
- Donlon, C. J., Minnett, P. J., Gentemann, C., Nightingale, T. J., Barton, I. J., Ward, B., & Murray, M. J. (2002). Toward improved validation of satellite sea surface skin temperature measurements for climate research. *Journal of Climate*, 15, 353–369. [https://doi.org/10.1175/1520-0442\(2002\)015\(0353:TIVOSS\)2.0.CO;2](https://doi.org/10.1175/1520-0442(2002)015(0353:TIVOSS)2.0.CO;2)
- Eastwood, S., Le Borgne, P., Péré, S., & Poulter, D. (2011). Diurnal variability in sea surface temperature in the Arctic. *Remote Sensing of Environment*, 115, 2594–2602. <https://doi.org/10.1016/j.rse.2011.05.015>
- Embury, O. (2024). ESA Sea Surface Temperature Climate Change Initiative (SST\_cci): Advanced Very High Resolution Radiometer (AVHRR) Level 3 Collated (L3C) product, version 3.0. NERC EDS Centre for Environmental Data Analysis [Dataset]. <https://doi.org/10.5285/be418645dfa542df86165a7caad24284>
- Embury, O., Bulgin, C. E., & Mittaz, J. (2019). ESA Sea Surface Temperature Climate Change Initiative (SST\_cci): Along-Track Scanning Radiometer (ATSR) Level 3 Collated (L3C) Climate Data Record, version 2.1. Centre for Environmental Data Analysis [Dataset]. <https://doi.org/10.5285/5db2099606b94e63879d841c87e654ae>
- Embury, O., Merchant, C. J., Good, S. A., Rayner, N. A., Høyer, J. L., Atkinson, C., et al. (2024). Satellite-based time-series of sea-surface temperature since 1980 for climate applications. *Scientific Data*, 11(326), 326. <https://doi.org/10.1038/s41597-024-03147-w>
- Esters, L., Breivik, O., Landwehr, S., ten Doeschate, A., Sutherland, G., Christensen, K. H., et al. (2018). Turbulence scaling comparisons in the ocean surface boundary layer. *Journal of Geophysical Research: Oceans*, 123(3), 1–20. <https://doi.org/10.1002/2017JC013525>
- Esters, L., Landwehr, S., Sutherland, G., Bell, T. G., Christensen, K. H., Saltzman, E. S., et al. (2017). Parameterizing air-sea gas transfer velocity with dissipation. *Journal of Geophysical Research: Oceans*, 122(4), 3041–3056. <https://doi.org/10.1002/2016JC012088>
- Fairall, C. W., Bradley, E. F., Godfrey, J. S., Wick, G. A., Edson, J. B., & Young, G. S. (1996). Cool-skin and warm-layer effects on sea surface temperature. *Journal of Geophysical Research*, 101(C1), 1295–1308. <https://doi.org/10.1029/95jc03190>
- Fairall, C. W., Bradley, E. F., Hare, J. E., Grachev, A. A., & Edson, J. B. (2003). Bulk parameterization of air-sea fluxes: Updates and verification for the COARE algorithm. *Journal of Climate*, 16(4), 571–591. [https://doi.org/10.1175/1520-0442\(2003\)016<0571:bpoasf>2.0.co;2](https://doi.org/10.1175/1520-0442(2003)016<0571:bpoasf>2.0.co;2)
- Flament, P., Firing, J., Sawyer, M., & Trefois, C. (1994). Amplitude and horizontal structure of a large diurnal sea surface warming event during the coastal ocean dynamics experiment. *Journal of Physical Oceanography*, 24, 124–139.
- Gentemann, C. L. (2014). Three way validation of MODIS and AMSR-E sea surface temperatures. *Journal of Geophysical Research: Oceans*, 119(4), 2583–2598. <https://doi.org/10.1002/2013JC009716>
- Gentemann, C. L., Donlon, C. J., Stuart-Menteth, A., & Wentz, F. J. (2003). Diurnal signals in satellite sea surface temperature measurements. *Geophysical Research Letters*, 30(30). <https://doi.org/10.1029/2002GL016291>
- Gentemann, C. L., Minnett, P. J., Le Borgne, P., & Merchant, C. J. (2008). Multi-satellite measurements of large diurnal warming events. *Geophysical Research Letters*, 35(22), L22602. <https://doi.org/10.1029/2008GL035730>
- Giglio, D., Gille, S. T., Subramanian, A. C., & Nguyen, S. (2017). The role of wind gusts in upper ocean diurnal variability. *Journal of Geophysical Research: Oceans*, 122(9), 7751–7764. <https://doi.org/10.1002/2017JC012794>

- Giunta, V., & Ward, B. (2022). Ocean mixed layer depth from dissipation. *Journal of Geophysical Research: Oceans*, 127(4), e2021JC017904. <https://doi.org/10.1029/2021JC017904>
- Gorter, W., van Angelen, J. H., Lenaerts, J. T. M., & van den Broeke, M. R. (2014). Present and future near-surface wind climate of Greenland from high resolution regional climate modelling. *Climate Dynamics*, 42(5), 1595–1611. <https://doi.org/10.1007/s00382-013-1861-2>
- Hersbach, H., Bell, B., Berrisford, P., Biavati, G., Horányi, A., Sabater, J. M., et al. (2023). ERA5 hourly data on single levels from 1940 to present [Dataset]. *Copernicus Climate Change Service (C3S) Climate Data Store (CDS)*. <https://doi.org/10.24381/cds.adbb2d47>
- Hogan, L., Zappa, C. J., Cifuentes-Lorenzen, A., Edson, J. B., O'Donnell, J., & Ullman, D. S. (2025). Observations of breaking wave dissipation and their relationship to atmosphere-ocean energy transfer. *Journal of Geophysical Research: Oceans*, 130, e2024JC022130. <https://doi.org/10.1029/2024JC022130>
- Hsu, J.-Y., Chang, M.-H., Jan, S., & Yang, Y. J. (2024). Synergistic impact of diurnal warm layers and inertial wave mixing on sea surface temperature warming and upper ocean stratification. *Journal of Geophysical Research: Oceans*, 129(11), e2023JC020623. <https://doi.org/10.1029/2023JC020623>
- Jia, C., Minnett, P. J., & Luo, B. (2023). Significant diurnal warming events observed by Saildrone at high latitudes. *Journal of Geophysical Research: Oceans*, 128(1), e2022JC019368. <https://doi.org/10.1029/2022JC019368>
- Kara, A. B., Wallcraft, A. J., & Hurlburt, H. E. (2005). A new solar radiation penetration scheme for use in ocean mixed layer studies: An application to the Black Sea using a fine-resolution hybrid coordinate ocean model (HYCOM). *Journal of Physical Oceanography*, 35(1), 13–32. <https://doi.org/10.1175/jpo2677.1>
- Kawai, Y., & Kawamura, H. (2000). Study on a platform effect in the in situ sea surface temperature observations under weak wind and clear sky conditions using numerical models. *Journal of Atmospheric and Oceanic Technology*, 17(2), 185–196. [https://doi.org/10.1175/1520-0426\(2000\)017<0185:soapei>2.0.co;2](https://doi.org/10.1175/1520-0426(2000)017<0185:soapei>2.0.co;2)
- Kawai, Y., & Kawamura, H. (2002). Evaluation of the diurnal warming of sea surface temperature using satellite-derived marine meteorological data. *Journal of Oceanography*, 58(6), 805–814. <https://doi.org/10.1023/a:1022867028876>
- Kawai, Y., Kawamura, H., Tanba, S., Ando, K., Yoneyama, K., & Nagahama, N. (2006). Validity of sea surface temperature observed with the TRITON buoy under diurnal heating conditions. *Journal of Oceanography*, 62(6), 825–838. <https://doi.org/10.1007/s10872-006-0101-3>
- Kawai, Y., & Wada, A. (2007). Diurnal sea surface temperature variation and its impact on the atmosphere and ocean: A review. *Journal of Oceanography*, 63(5), 721–744. <https://doi.org/10.1007/s10872-007-0063-0>
- Kennedy, J. J., Brohan, P., & Tett, S. F. B. (2007). A global climatology of the diurnal variations in sea-surface temperature and implications for MSU temperature trends. *Geophysical Research Letters*, 34(L05712). <https://doi.org/10.1029/2006GL028920>
- Kettle, H., Merchant, C. J., Jeffery, C. D., Filipiak, M. J., & Gentemann, C. L. (2009). The impact of diurnal variability in sea surface temperature on the central Atlantic air-sea CO<sub>2</sub> flux. *Atmospheric Chemistry and Physics*, 9(2), 529–541. <https://doi.org/10.5194/acp-9-529-2009>
- Kukulka, T., Plueddemann, A. J., & Sullivan, P. P. (2013). Inhibited upper ocean restratification in nonequilibrium swell conditions. *Geophysical Research Letters*, 40(14), 3672–3676. <https://doi.org/10.1002/grl.50708>
- Lamont, J. C., & Scott, D. S. (1970). An eddy cell model of mass transfer into the surface of a turbulent liquid. *AIChE Journal*, 16(4), 513–519. <https://doi.org/10.1002/aic.690160403>
- Le Boyer, A., Couto, N., Alford, M. H., Drake, H. F., Bluteau, C. E., Hughes, K. G., et al. (2023). Turbulent diapycnal fluxes as a pilot essential ocean variable. *Frontiers in Marine Science*, 10, 1241023. <https://doi.org/10.3389/fmars.2023.1241023>
- Liu, M., Merchant, C. J., Embury, O., Liu, J., Song, Q., & Guan, L. (2022). Retrieval of sea surface temperature from HY-1B COCTS. *IEEE Transactions on Geoscience and Remote Sensing*, 60, 1–13. <https://doi.org/10.1109/TGRS.2022.3190444>
- Loeb, N. G., Wielicki, B. A., Doelling, D. R., Smith, G. L., Keyes, D. F., Kato, S., et al. (2009). Toward optimal closure of the Earth's top-of-atmosphere radiation budget. *Journal of Climate*, 22(3), 748–766. <https://doi.org/10.1175/2008JCL2637.1>
- Lombardo, C. P., & Gregg, M. C. (1989). Similarity scaling of viscous and thermal dissipation in a convecting surface boundary layer. *Journal of Geophysical Research*, 94(C5), 6273–6284. <https://doi.org/10.1029/jc094ic05p06273>
- Matthews, A. J., Baranowski, D. B., Heywood, K. J., Flatau, P. J., & Schmidtko, S. (2014). The surface diurnal warm layer in the Indian Ocean during CINDY/DYNAMO. *Journal of Climate*, 27(24), 9101–9122. <https://doi.org/10.1175/JCLI-D-14-00222.1>
- Matthews, J. L., Peng, G., Meier, W. N., & Brown, O. (2020). Sensitivity of arctic sea ice extent to sea ice concentration threshold choice and its implication to ice coverage decadal trends and statistical projections. *Remote Sensing*, 12(5), 807. <https://doi.org/10.3390/rs12050807>
- Maturi, E., Harris, A., Merchant, C. J., Mittaz, J., Potash, B., Meng, W., & Sapper, J. (2008). NOAA's sea surface temperature products from operational geostationary satellites. *Bulletin American Meteorology Social*, 89(12), 1877–1888. <https://doi.org/10.1175/2008BAMS2528.1>
- McNeil, C. L., & Merlivat, L. (1996). The warm oceanic surface layer: Implications for CO<sub>2</sub> fluxes and surface gas measurements. *Geophysical Research Letters*, 23(24), 3575–3578. <https://doi.org/10.1029/96gl03426>
- Merchant, C. J., Embury, O., Bulgin, C. E., Block, T., Corlett, G. K., Fiedler, E., et al. (2019). Satellite-based time-series of sea-surface temperature since 1981 for climate applications. *Scientific Data*, 6(223), 223. <https://doi.org/10.1038/s41597-019-0236-x>
- Merchant, C. J., Filipiak, M. J., Borgne, P. L., Roquet, H., Autret, E., Piollé, J.-F., & Lavender, S. (2008). Diurnal warm-layer events in the western Mediterranean and European shelf seas. *Geophysical Research Letters*, 35(L04601). <https://doi.org/10.1029/2007GL030371>
- Min, H. S., & Noh, Y. (2004). Influence of the surface heating on Langmuir circulation. *Journal of Physical Oceanography*, 34(12), 2630–2641. <https://doi.org/10.1175/JPOJPO-2654.1>
- Moulin, A. J., Moum, J. N., & Shroyer, E. L. (2018). Evolution of turbulence in the diurnal warm layer. *Journal of Physical Oceanography*, 48(2), 383–396. <https://doi.org/10.1175/JPO-D-17-0170.1>
- Naustvoll, L. J., Melle, W., Klevjer, T., Drinkwater, K. F., Strand, E., & Knutsen, T. (2020). Dynamics of phytoplankton species composition, biomass and nutrients in the north Atlantic during spring and summer - A trans-Atlantic study. *Deep Sea Research Part II: Topical Studies in Oceanography*, 180, 104890. <https://doi.org/10.1016/j.dsr2.2020.104890>
- NOAA CoastWatch. (2024). ACSPO MODIS SST data produced from Terra and Aqua satellites, L3C (level 3 collated) [Dataset]. Retrieved from <https://coastwatch.noaa.gov/pub/socd2/coastwatch/sst/ran/modis/>
- Noh, Y., Goh, G., Raasch, S., & Gryschka, M. (2009). Formation of a diurnal thermocline in the Ocean mixed layer simulated by LES. *Journal of Physical Oceanography*, 39(5), 1244–1257. <https://doi.org/10.1175/2008JPO4032.1>
- Ocean and Sea Ice Satellite Application Facility (OSI SAF). (2015). GHRSSST Level 3C sub-skin Sea Surface Temperature from the Geostationary Operational Environmental Satellites (GOES 13) Imager in East position produced by OSI SAF (GDS version 2) [Dataset]. Retrieved from <https://podaac.jpl.nasa.gov/dataset/GOES13-OSISAF-L3C-v1.0>
- Price, J. F., Weller, R. A., & Pinkel, R. (1986). Diurnal cycling: Observations and models of the upper ocean response to diurnal heating, cooling, and wind mixing. *Journal of Geophysical Research*, 91(C7), 8411–8427. <https://doi.org/10.1029/jc091ic07p08411>
- Remote Sensing Systems. (2014). GHRSSST Level 2P Global Subskin SST from the AMSR-E. Ver. 7a. PO.DAAC, CA, USA [Dataset]. <https://doi.org/10.5067/GHAMS-2GR07>

- Remote Sensing Systems. (2017). GHRSSST Level 3U Global Subskin SST from the AMSR-E. Ver. 7a. PO.DAAC, CA, USA [Dataset]. <https://doi.org/10.5067/GHAMS-3GR7A>
- Shcherbina, A. Y., D'Asaro, E. A., & Harcourt, R. R. (2019). Rain and sun create slippery layers in eastern Pacific fresh pool. *Oceanography*, 32(2), 98–107. <https://doi.org/10.5670/oceanog.2019.217>
- Soloviev, A., & Lukas, R. (1997). Observation of large diurnal warming events in the near-surface layer of the western equatorial Pacific warm pool. *Deep-Sea Research I*, 44(6), 1055–1076. [https://doi.org/10.1016/S0967-0637\(96\)00124-0](https://doi.org/10.1016/S0967-0637(96)00124-0)
- Stuart-Menteth, A. C., Robinson, I. S., & Challenor, P. G. (2003). A global study of diurnal warming using satellite-derived sea surface temperature. *Journal of Geophysical Research*, 108(C5). <https://doi.org/10.1029/2002JC001534>
- Stuart-Menteth, A. C., Robinson, I. S., Weller, R. A., & Donlon, C. J. (2005). Sensitivity of the diurnal warm layer to meteorological fluctuations part 1: Observations. *Journal of Atmospheric and Oceanic Science*, 10(3), 193–208. <https://doi.org/10.1080/17417530500529521>
- Sutherland, G., Marié, L., Reverdin, G., Christensen, K. H., Broström, G., & Ward, B. (2016). Enhanced turbulence associated with the diurnal jet in the ocean surface boundary layer. *Journal of Physical Oceanography*, 46, 3051–3067. <https://doi.org/10.1175/JPO-D-15-0172.1>
- Sutherland, G., Reverdin, G., Marié, L., & Ward, B. (2014). Mixed and mixing layer depths in the ocean surface boundary layer under conditions of diurnal stratification. *Geophysical Research Letters*, 41(23), 8469–8476. <https://doi.org/10.1002/2014GL061939>
- Sverdrup, H. U., Johnson, M. W., & Fleming, R. H. (1942). *The oceans their physics, chemistry, and general biology*. Prentice-Hall.
- Thierry, V., Claustre, H., Pasqueron de Fommervault, O., Zilberman, N., Johnson, K. S., King, B. A., et al. (2025). Advancing ocean monitoring and knowledge for societal benefit: The urgency to expand Argo to OneArgo by 2030. *Frontiers in Marine Science*, 12, 1593904. <https://doi.org/10.3389/fmars.2025.1593904>
- Tokoro, T., Kayanne, H., Watanabe, A., Nadaoka, K., Tamura, H., Nozaki, K., et al. (2008). High gas-transfer velocity in coastal regions with high energy-dissipation rates. *Journal of Geophysical Research*, 113(C11), C11006. <https://doi.org/10.1029/2007JC004528>
- Wain, D. J., Lilly, J. M., Callaghan, A. H., Yashayaev, I., & Ward, B. (2015). A breaking internal wave in the surface ocean boundary layer. *Journal of Geophysical Research: Oceans*, 120(6), 4151–4161. <https://doi.org/10.1002/2014JC010416>
- Ward, B. (2006). Near-surface ocean temperature. *Journal of Geophysical Research*, 111(C02004). <https://doi.org/10.1029/2004JC002689>
- Ward, B., & Donelan, M. A. (2006). Thermometric measurements of the molecular sublayer at the air-water interface. *Geophysical Research Letters*, 33(7). <https://doi.org/10.1029/2005GL024769>
- Ward, B., Fristedt, T., Callaghan, A. H., Sutherland, G., Sanchez, X., Vialard, J., & ten Doeschate, A. (2014). The Air-Sea Interaction Profiler (ASIP): An autonomous upwardly rising profiler for microstructure measurements in the upper ocean. *Journal of Atmospheric and Oceanic Technology*, 31(10), 2246–2267. <https://doi.org/10.1175/JTECH-D-14-00010.1>
- Ward, B., & Hauser, S. F. (2025). Dataset for JGR-oceans article 2025JC022918: In-situ observation of a strong diurnal warming event in the Labrador Sea undetected by satellites (1.0) [Dataset]. *Zenodo*. <https://doi.org/10.5281/zenodo.17580777>
- Ward, B., Wanninkhof, R., Minnett, P. J., & Head, M. J. (2004). SkinDeEP: A profiling instrument for upper-decimeter sea surface measurements. *Journal of Atmospheric and Oceanic Technology*, 21(2), 207–222. [https://doi.org/10.1175/1520-0426\(2004\)021<0207:sapifu>2.0.co;2](https://doi.org/10.1175/1520-0426(2004)021<0207:sapifu>2.0.co;2)
- Warren, S. G., Hahn, C. J., London, J., Chervin, R. M., & Jenne, R. L. (1988). Global distribution of total cloud cover and cloud type amounts over the ocean. NCAR Tech. Note NCAR/TN-317-STR. <https://doi.org/10.2172/5415329>
- Webster, P. J., Clayson, C. A., & Curry, J. A. (1996). Clouds, radiation, and the diurnal cycle of sea surface temperature in the tropical Western Pacific. *Journal of Climate*, 9(8), 1712–1730. [https://doi.org/10.1175/1520-0442\(1996\)009<1712:craatdc>2.0.co;2](https://doi.org/10.1175/1520-0442(1996)009<1712:craatdc>2.0.co;2)
- Wick, G. A., & Castro, S. L. (2020). Assessment of extreme diurnal warming in operational geosynchronous satellite sea surface temperature products. *Remote Sensing*, 12(22), 3771. <https://doi.org/10.3390/rs12223771>
- Wick, G. A., Castro, S. L., Harris, A., & Mittaz, J. (2024). Evaluation of modeled diurnal warming estimates for application to producing sea surface temperature analyses. *Earth and Space Science*, 11(9), e2024EA003619. <https://doi.org/10.1029/2024EA003619>
- Wielicki, B., Cess, R. D., King, M. D., Randall, D. A., & Harrison, E. F. (1995). Mission to planet Earth: Role of clouds and radiation in climate. *Bulletin of the American Meteorological Society*, 76(11), 2125–2153. [https://doi.org/10.1175/1520-0477\(1995\)076<2125:mtpero>2.0.co;2](https://doi.org/10.1175/1520-0477(1995)076<2125:mtpero>2.0.co;2)
- Woolf, D. K., Land, P. E., Shutler, J. D., Goddijn-Murphy, L. M., & Donlon, C. J. (2016). On the calculation of air-sea fluxes of CO<sub>2</sub> in the presence of temperature and salinity gradients. *Journal of Geophysical Research: Oceans*, 121(2), 1229–1248. <https://doi.org/10.1002/2015JC011427>
- Yashayaev, I., Lazier, J. R. N., & Clarke, R. A. (2003). Temperature and salinity in the central Labrador Sea during the 1990s and in the context of the longer-term change. *Marine Science Symposia*, 219. <https://doi.org/10.17895/ices.pub.19271729.v1>
- Yashayaev, I., & Loder, J. W. (2016). Recurrent replenishment of Labrador Sea Water and associated decadal-scale variability. *Journal of Physical Oceanography*, 121(11), 8095–8114. <https://doi.org/10.1002/2016JC012046>
- Yashayaev, I., & Loder, J. W. (2017). Further intensification of deep convection in the Labrador Sea in 2016. *Geophysical Research Letters*, 44(3), 1429–1438. <https://doi.org/10.1002/2016GL071668>
- Zappa, C. J., McGillis, W. R., Raymond, P. A., Edson, J. B., Hints, E. J., Zemmeling, H. J., et al. (2007). Environmental turbulent mixing controls on air-water gas exchange in marine and aquatic systems. *Geophysical Research Letters*, 34(L10601). <https://doi.org/10.1029/2006GL028790>
- Zeiden, K., Thomson, J., Shcherbina, A., & D'Asaro, E. (2024). Observations of elevated mixing and periodic structures within diurnal warm layers. *Journal of Geophysical Research: Oceans*, 129(11), e2024JC021399. <https://doi.org/10.1029/2024JC021399>